2010

Determining the Error Characteristics of H*WIND

Steven Dinapoli

THE FLORIDA STATE UNIVERSITY

COLLEGE OF ARTS AND SCIENCES

DETERMINING THE ERROR CHARACTERISTICS OF H*WIND

By

STEVEN DINAPOLI

A thesis submitted to the
Department of Earth, Ocean, and Atmospheric Science
in partial fulfillment of the
requirements for the degree of
Master of Science

Degree Awarded:
Fall Semester, 2010

The members of the Committee approve the thesis of Steven DiNapoli defended on October 8, 2010.

_____
Mark Bourassa
Professor Directing Thesis

_____
Mark Powell
Committee Member

_____
Robert Hart
Committee Member

_____
Guosheng Liu
Committee Member

The Graduate School has verified and approved the above-named committee members

ACKNOWLEDGEMENTS

I would like to thank my major professor, Dr. Mark Bourassa, for all of the hard work he has done in support of my thesis work. He has guided me through every step of my research and his expertise has proven to be invaluable. I would also like to thank Drs. Mark Powell, Robert Hart, and Guosheng Liu for serving on my Master's committee. All of them have been extremely helpful, especially Mark Powell, who shared with me his vast expertise on H*Wind. Finally, I would like to thank Drs. Eric Uhlhorn and Bradley Klotz of the NOAA Hurricane Research Division for sharing their knowledge of tropical cyclone observations at the 2010 AMS Tropical Meteorology Conference.

TABLE OF CONTENTS

LIST OF FIGURES

ABSTRACT

The HRD Real-time Hurricane Wind Analysis System (H*Wind) is a software application used by NOAA's Hurricane Research Division to create a gridded tropical cyclone wind analysis based on a wide range of observations. One application of H*Wind fields is calibration of scatterometers for high wind speed environments. Unfortunately, the accuracy of the H*Wind product has not been studied extensively, and therefore the accuracy of scatterometer calibrations in these environments is also unknown. This investigation seeks to determine the uncertainty in the H*Wind product and estimate the contributions of several potential error sources. These error sources include random observation errors, relative bias between different data types, temporal drift resulting from combining non-simultaneous measurements, and smoothing and interpolation errors in the H*Wind software.

The effects of relative bias between different data types and random observation errors are determined by performing statistical calculations on the observed wind speeds. We show that in the absence of large biases, the total contribution of all error sources results in an uncertainty of approximately 7% near the storm center, which increases to nearly 15% near the tropical storm force wind radius. The H*Wind analysis algorithm is found to introduce a positive bias to the wind speeds near the storm center, where the analyzed wind speeds are enhanced to match the highest observations. In addition, spectral analyses are performed to ensure that the filter wavelength of the final analysis product matches user specifications. With increased knowledge of these error sources and their effects, researchers will have a better understanding of the uncertainty in the H*Wind product, and can then judge the suitability of H*Wind for various research applications.

CHAPTER 1

INTRODUCTION

Over the past several years, vast improvements in observations, computing power, and objective analysis techniques (e.g., ensemble Kalman filters) have enabled scientists to generate gridded analyses of tropical cyclone wind fields. These analyses have several practical uses in both forecasting and research applications. Forecasters can use near real-time analyses to analyze the spatial extent of the surface wind field and to determine the storm surge threat of an approaching system (Powell and Houston 1996; Morey et al. 2006). This information can then be passed to emergency managers, who can make timely evacuation orders and thus minimize the loss of life. Researchers can use gridded products for post-storm reanalysis (Landsea et al. 2004; Powell et al. 2009), analysis of storm structure (Vickery and Wadhera 2008), and modeling applications (Halliwell et al. 2008; Xiao et al. 2009).

The NOAA Hurricane Research Division's Hurricane Wind Analysis System (H*Wind; Powell et al. 1998; Powell et al. 2009) is a gridded analysis product that is available both in real-time and for historical cases. The H*Wind software produces a gridded analysis by interpolating and smoothing wind speed observations from multiple platforms. Unfortunately, no extensive uncertainty analysis has been performed on the H*Wind analysis product; therefore, unknown error quantities are being introduced in applications in which H*Wind is utilized. The lack of scientific understanding of these errors and their magnitudes has limited its usefulness in numerous scientific applications.

This study investigates the sources of uncertainty in H*Wind and seeks to determine their impacts on the gridded product. These sources can be categorized into two basic groups. The first group consists of observation errors, including random data errors and relative biases between different data types. The contributions of these uncertainties are determined by analyzing the biases and variances of each type of observation data. The second group contains errors introduced by the data assimilation techniques in H*Wind, including height adjustment errors, smoothing and interpolation errors, and systematic biases. A spectral analysis is performed to determine the effects of smoothing, and systematic biases are detected by comparing the H*Wind analyses with the individual observations. With an understanding of these error sources, researchers and forecasters will have better uncertainty estimates for tropical cyclone wind fields, and improvements can be made to the H*Wind algorithm to correct systematic errors.

CHAPTER 2

H*WIND OVERVIEW

The H*Wind application contains an extensive database of tropical cyclone wind observations from the year 2000 onwards. This database contains observations from a vast array of marine, land, aircraft, and satellite platforms. The user selects a storm and a time frame to perform the analysis, and H*Wind retrieves the corresponding observations from its database. The winds from each observation platform are automatically adjusted to a 1-minute average at a 10m height based on an open marine exposure as described below in Section 2.1; however, users can also make manual adjustments or alter the adjustment schemes if necessary.

2.1 Data Types and Adjustments

Data from the NOAA stepped frequency microwave radiometer (SFMR) are considered to be among the most accurate marine wind observations (Powell et al. 2009), and are therefore used in H*Wind analyses when available. Two NOAA aircraft are equipped with SFMR instrumentation, which measures microwave emission from the ocean surface to determine the wind speed. Adjustment of the SFMR data is based on a calibration that was performed in 2004 and 2005 (Uhlhorn and Black 2003; Uhlhorn et al. 2007).

In the absence of SFMR data, surface-adjusted flight level winds are preferred due to their high density and reasonably low uncertainty. These observations are adjusted to a 10 m height using the method described by Powell et al. (2009). This adjustment method is based on comparisons of radial wind profiles from flight level and SFMR data. The adjusted flight level winds are compared to nearby surface observations and manual alterations are made to the adjustment scheme if large discrepancies are found.

Observations from GPS dropsondes, ships, and buoys are limited in quantity, but they all provide useful surface data for H*Wind analyses when available. The dropsonde data is adjusted to a 1-minute average 10 m wind by calculating the mean wind speed in the lowest 150 m of the boundary layer and adjusting using the technique developed by Franklin et al. (2003). All other marine-based data is adjusted to a standard height of 10m using a surface layer model (Liu et al. 1979), assumed to represent a 10-minute mean wind. The maximum 1-minute wind is then obtained by multiplying by a gust factor equal to 1.1 (Powell et al. 2009).

Satellite observations are available from QuikSCAT's SeaWinds scatterometer and from tracking low level cloud movements in GOES visible imagery. These observations provide high-density data near the outer fringes of tropical cyclones, where observations are otherwise quite sparse. Closer to the center of tropical cyclones, the QuikSCAT observations are less useful because of serious contamination from clouds and rain. QuikSCAT contains an internal rain-flagging algorithm that highlights these severely contaminated observations so they can easily be removed from the H*Wind analysis. The standardization processes for these satellites are described by Powell et al. (1996) and Dunion et al. (2002).

The primary land-based observation platforms used in H*Wind analyses include reports from aviation weather (METAR) and Automated Surface Observing System (ASOS) stations. Wind speeds observed from these platforms are heavily influenced by local and upstream terrain

features. Roughness parameters are therefore estimated for each station, and the observations are standardized to a marine exposure as described by Powell et al. (2009).

2.2 Generating the Analyses

Once all of the data is obtained and adjusted to a common framework, H*Wind plots each observation in a storm-relative reference frame. This procedure requires knowledge of the storm track during the analysis period. H*Wind contains storm track data based on best track archives and various reconnaissance fixes, although it is frequently necessary to make adjustments and interpolations. For example, the best track coordinates are rounded to the nearest tenth of a degree, often resulting in unrealistic kinks in the track that must be removed. Once all of the observations are plotted in a storm-relative reference frame (figure 1), the user selects which data types to include in the analysis. In addition, the user inspects the observations and flags any non-representative data for removal from the analysis.

The H*Wind system produces a gridded analysis by smoothing and interpolating the available wind observations along with a series of interpolated bogus points using a cubic B spline interpolation scheme that minimizes the least square difference between the observations

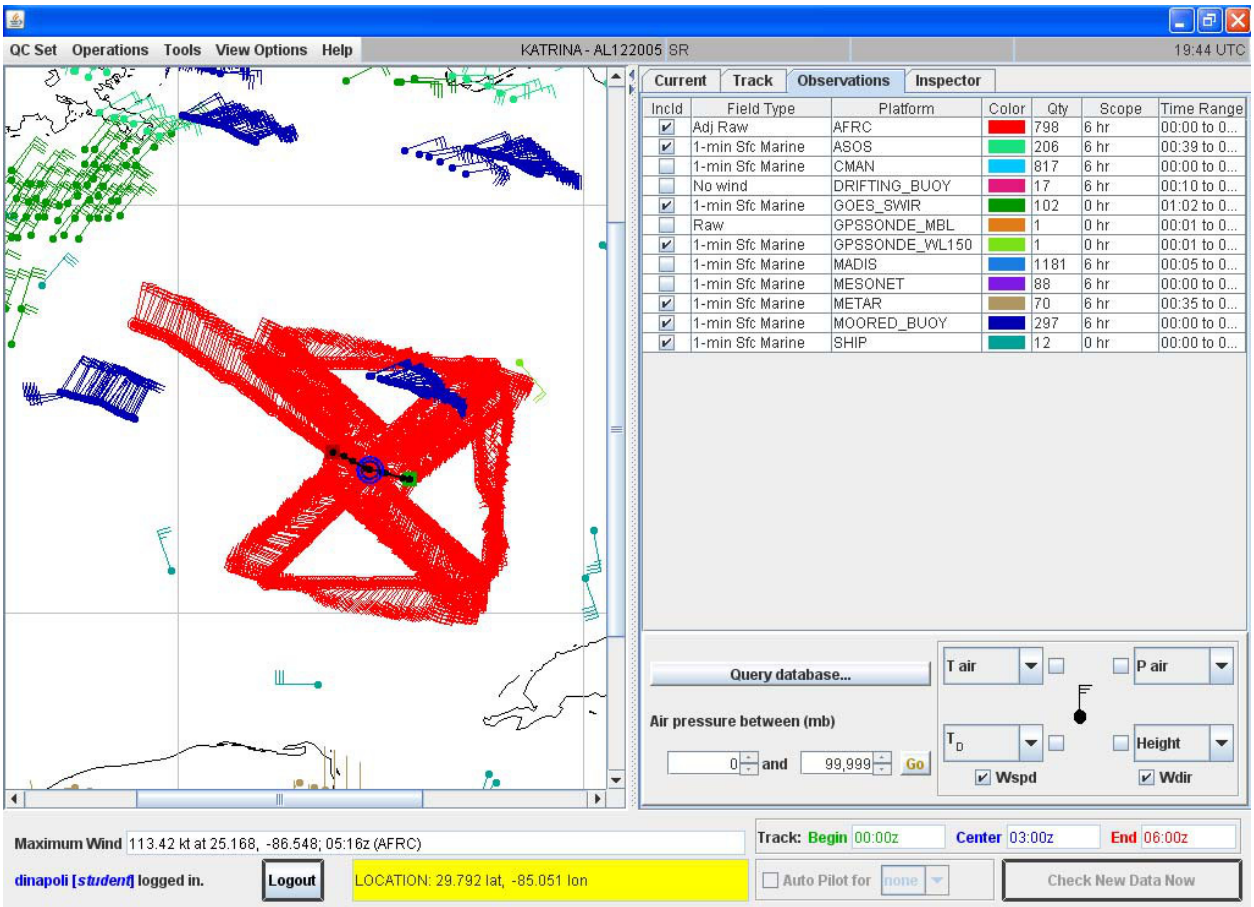

Figure 1: The H*Wind user interface. The observations are plotted in storm-relative coordinates, and each observation type is assigned its own color. The storm track is plotted in black, and the storm center at the analysis time is circled in blue.

and the analysis (Powell and Houston 1996). This scheme consists of five superimposed meshes, each with a unique filter wavelength. The filter wavelength is smallest in the innermost mesh, allowing for the finest scale resolution. In the outer meshes, the filter wavelength is considerably larger due to the decreased observation density. Each observation and bogus point is given a default weight between zero and one, with the most accurate and dense data platforms receiving the largest weights (Franklin et al. 1993). The sizes and filter wavelengths of the meshes, the weights of each observation type, and the distribution of bogus points can be modified by the user if necessary. Finally, H*Wind enhances the wind speeds near the eyewall to ensure that the peak observed wind speed is represented in the analysis. This enhancement is radially symmetric as a percentage change in wind speed, and it decreases exponentially with distance from the eyewall so that the outer wind radii are not overestimated (Powell 2010, personal communication). The resulting H*Wind analysis is shown in figure 3. In addition to the contour plot and wind radii pictured, H*Wind also returns the location and magnitude of the maximum observed and analyzed wind speeds, as well as the mean bias and root mean square difference between the analysis and the observations.

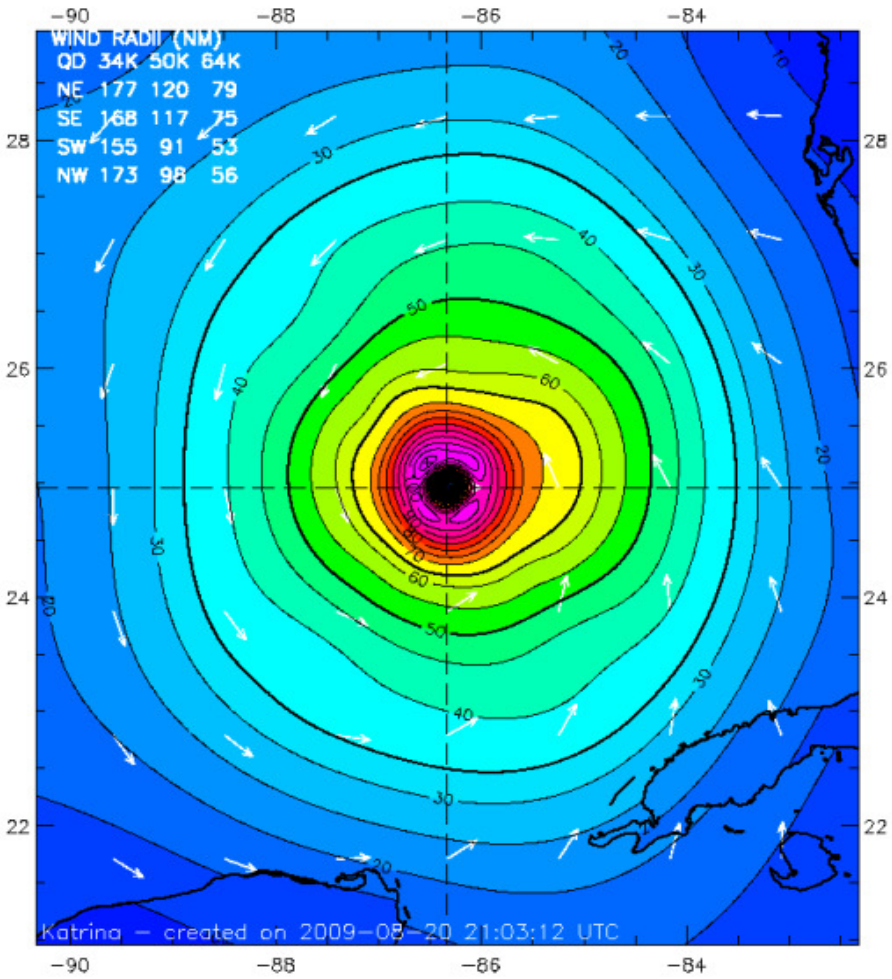

Figure 2: Example of H*Wind output. Wind speeds of Hurricane Katrina are contoured, and several important wind radii are noted on the top-left.

CHAPTER 3

DATA AND METHODS

The first analysis performed is a comparison of the observations with each other and with the H*Wind analyses to determine the amount of bias and uncertainty in the various data types. First, a series of H*Wind analyses is generated using the H*Wind program. After being quality-controlled, the analysis and observation wind speeds are binned by radius so that the bias and uncertainty can be calculated in each bin. Since the individual storm analyses do not have enough data to obtain statistically significant results for each individual data type, the analyses are combined into a larger dataset, which requires scaling the wind speeds and radial position to non-dimensional numbers to avoid adding unwanted variability.

The H*Wind program is used to generate a set consisting of 80 analyses from Hurricanes Charley and Ivan in 2004; Katrina, Rita and Wilma in 2005; and Felix in 2008. This data set contains storms with a wide array of sizes, intensities, and eye radii. Analyses are created every six hours while the tropical cyclone maintains at least hurricane intensity, assuming aircraft reconnaissance and/or stepped frequency radiometer data are available. Each analysis contains a six hour window of observation data, which provides enough time for reconnaissance aircraft to sample the storm, while attempting to minimize temporal variability within the data. H*Wind assumes that all of the data is representative of the analysis time, which is defined by the center of the six-hour analysis window. The choices of time windows and analysis frequency ensure that no data are used in more than one analysis, which would cause observations to be counted multiple times in the results. Both the analyzed wind field and the 10 m adjusted observations are obtained for each analysis period.

Before any statistical evaluations are made, it is necessary to perform several quality control procedures on the data. First, all land-based observations are removed from the dataset. The increased surface roughness results in significantly lower wind speeds over land, which contaminates the statistics of the composite data. In addition, if there is a lack of observation coverage within a particular quadrant, the observations and analysis grid data from that quadrant are removed from the composite dataset. Radial profiles from each quadrant of the H*Wind analyses are then plotted alongside the observations to ensure that the analyses are representative of the data. A common issue is that several of the H*Wind analyses are unable to resolve concentric eyewalls. H*Wind easily resolves the primary eyewall as a result of its enhancement scheme at the radius of maximum wind, but the secondary peak is left unresolved (figure 3). Resolving this peak would require a substantially lower filter wavelength, which would introduce large amounts of noise to the analysis, especially in the tangential direction. Analyses that display this problem are therefore removed from the dataset to avoid contaminating the results.

After all of the necessary quality control procedures are completed, calculations are made to determine the uncertainties and biases of each observation platform. Ideally, H*Wind fields would be recalculated for each comparison to a data type, with the data type being examined excluded from the H*Wind analyses. Such an approach would avoid biases from the data type being examined; however, in the vast majority of cases the data are too sparse for such an approach. A binning approach is therefore used, which provides estimates of the large biases present in the observation data. Each storm is divided into ten radial bins, which compromises

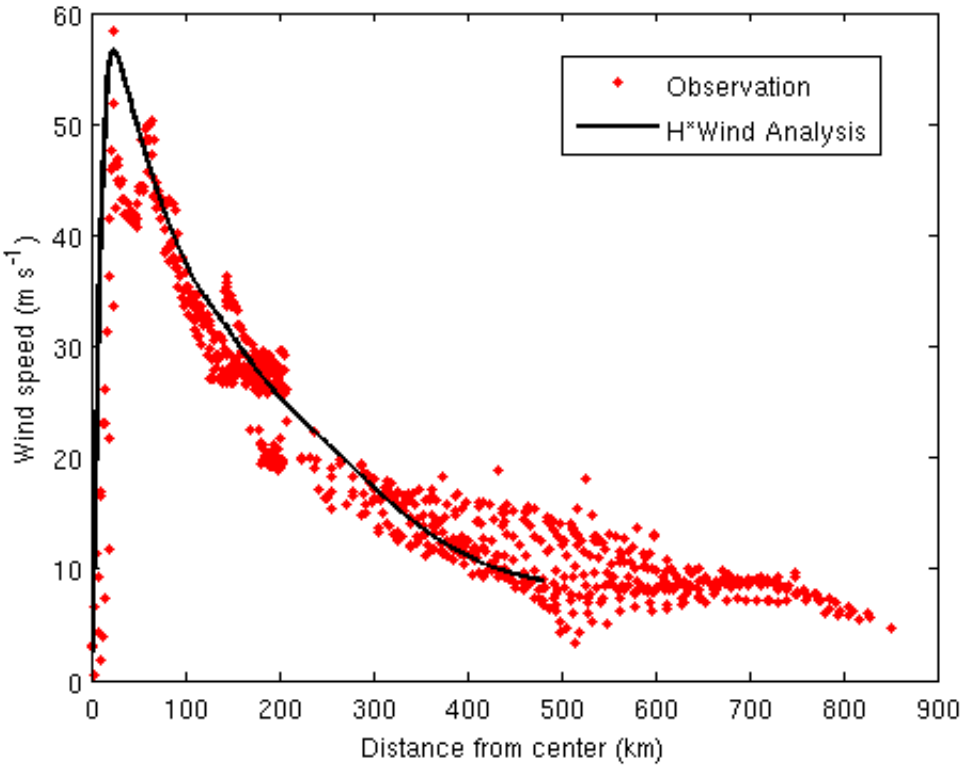

Figure 3: Comparison observations and H*Wind data. Observations from the right-rear quadrant of a 21Z 21 Oct 2005 analysis of Hurricane Wilma are plotted against a radial profile of the H*Wind analysis.

between ensuring that there is a significant number of observations in each bin and keeping the bin sizes small to minimize spatial variability. The first bin contains the observations inside the radius of maximum wind (R_{max}). This bin contains all of the variability associated with the eye, and is therefore excluded from most of the calculations. Outside of R_{max}, the observations are placed into the nine remaining bins, which are based on the relative position of the observations between R_{max} and the tropical storm force wind radius (R_{ts}). The cutoffs for each bin outside of R_{max} are equally spaced and calculated separately for each storm analysis and quadrant based on the values of R_{ts} minus R_{max}. Each bin therefore represents the same fraction of the distance between R_{max} and R_{ts} in each storm. Unfortunately, although there are adequate data in each bin to reassess the overall bias between the observations and H*Wind, there are not enough data available to obtain a statistically significant estimate of the biases between each individual observation platform. It is therefore necessary to combine data from multiple storm analyses to create a larger dataset.

CHAPTER 4

COMPOSITING THE ANALYSES

The lack of data required to obtain statistically significant estimates of the biases and random errors of each observation platform necessitates combining data from multiple storm analyses to increase the size of the dataset. This process could create large amounts of unwanted variability due to the different size and intensity characteristics of each individual storm. To minimize this unwanted variability, the wind speeds in each storm are scaled to a non-dimensional number by dividing by a parameterized radial wind profile. Various parameterization schemes (Holland 1980; Willoughby et al. 2003) exist to derive radial wind profiles. Unfortunately, the central and ambient pressure data needed to parameterize Holland profiles and the geopotential height data needed to fit Willoughby profiles are not readily available for every storm analysis. A neural network approach described below is therefore used to derive radial wind profiles given a set of very basic storm parameters that are easily retrieved from the wind observations and H*Wind analyses. An important consequence of this technique is that the profiles are based on mathematical fitting alone, and not on any physical constraints.

Figure 4 shows a schematic illustrating how the neural network is trained to derive radial wind profiles. First, the data from one half of the storm analyses is set aside for the specific purpose of training the network. To create this training dataset, the storm analyses are placed into three categories of intensity and size, with each category containing roughly one-third of the analyses. Storm analyses from each category of intensity and storm size are then manually placed in the training dataset, ensuring that storms with a wide spectrum of sizes and intensities are represented. Next, the observations and H*Wind analyses are used to calculate seven parameters for each quadrant of each analysis in the training dataset. The maximum wind speed and the radius of maximum wind are used to accurately represent the peak of the wind profile, and the maximum radius at which tropical storm force wind speeds occur is used to represent the size of each storm. The remaining four parameters are the wind speeds at two times and four

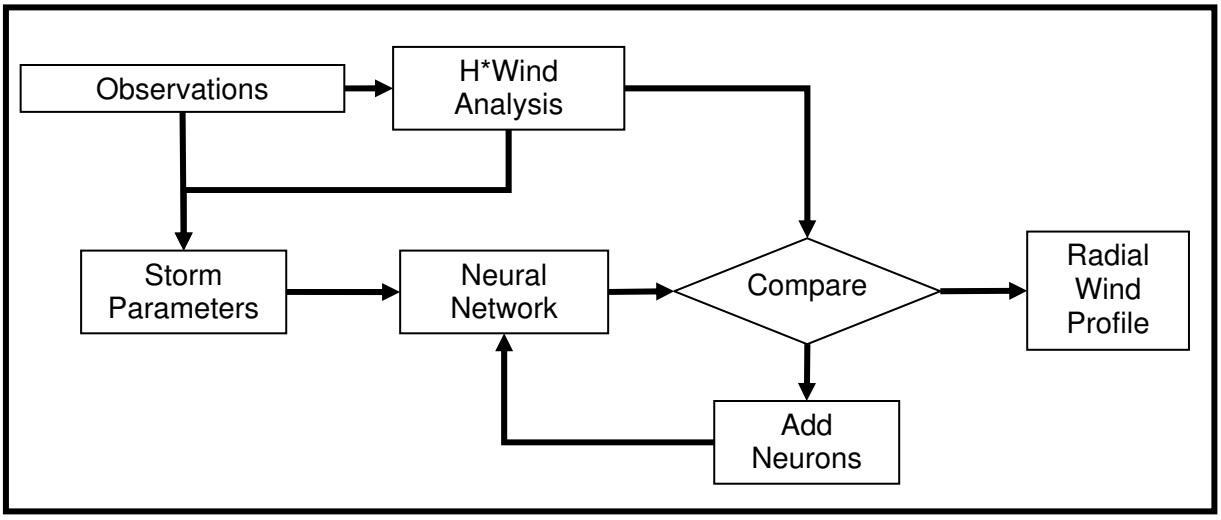

Figure 4: Schematic of the neural network algorithm

times the radius of maximum wind and the radius at which the wind speed decays to one-half and three-quarters of the maximum. These four parameters are selected to give an estimate of the radial decay rate outside of the eyewall.

Once all of the parameters are obtained, they are inputted into a radial basis neural network. The neural network algorithm used in this procedure is a part of the MATLAB Neural Network Toolbox. This algorithm consists of several simple operations, called neurons, acting in parallel to create a series of radial wind profiles. The network consists of two layers of neurons acting in series. The first layer is designed to weight each input, and is built iteratively, with one neuron being added in each iteration until the sum-squared error between the derived profiles and the corresponding H*Wind profiles falls below 0.5 m s^{-1}. Achieving lower sum-squared error values requires a large number of neurons, which in turn requires a larger number of data to configure the network. The output of the first layer is then passed to the second layer, which generates the wind profiles.

Each set of parameters is input into the network as an Nx7 matrix, where N is the number of input parameter sets (i.e., the number of storm profiles). Each neuron in the first layer of the neural network contains a 1x7 weight vector and a bias constant. The weight vector is set equal to the seven parameters of one of the input storms. The neuron calculates the magnitude of the vector difference between each row of the input matrix and the weight vector; each input storm is therefore assigned a value that represents its dissimilarity from the weight vector. These results are then multiplied by the bias constant, which is chosen so that the network responds adequately to changes in storm parameters. A bias constant that is too high results in the network being unable to handle parameters that are not close to those of a neuron's weight vector; however a low bias constant results in the network treating all input parameters similarly. A bias constant of 8.326×10^{-3} is empirically chosen to compromise between these two extremes. The resulting values are then passed through the transfer function

$$y = \exp(-x^2), \tag{1}$$

where x is the magnitude of the vector difference between a set of input parameters and the weight vector multiplied by the bias constant. This transfer function gives each storm a weight between zero and one, with the highest weights going to the storms whose parameters most closely match the weight vector. With the chosen bias constant, a vector difference magnitude of 100 yields a transfer function output of 0.5.

After passing through the transfer function, the results in each neuron enter into the second layer of the neural network in the form of a matrix. This layer also takes in a matrix containing profiles of each H*Wind analysis. These profiles consist of 50 evenly-spaced points between R_{max} and 1.5 times R_{ts}, as well as two points inside R_{max}. The second layer performs a least-square linear regression between the output of the first layer and the target H*Wind profiles. Once enough neurons are created for the sum-squared error to fall below 0.5 m s^{-1} the completed neural network is used to derive radial profiles for the remaining storm analyses.

Each of the neural network-derived radial profiles is plotted alongside the observations and the H*Wind profile from the respective storm to ensure that the neural network-derived profiles provide a reasonable fit (figure 5). Two of the profiles are deemed not to have a reasonable fit, and all data from those analyses are removed from the dataset. The remaining observations and H*Wind analysis grid points are scaled by dividing the observed wind speeds by wind speeds of the neural network at the corresponding radius. Since the neural network

profile is defined at only 52 points, wind speeds at radii in between these points are calculated using a cubic spline interpolation. The resulting non-dimensional winds are used to estimate the

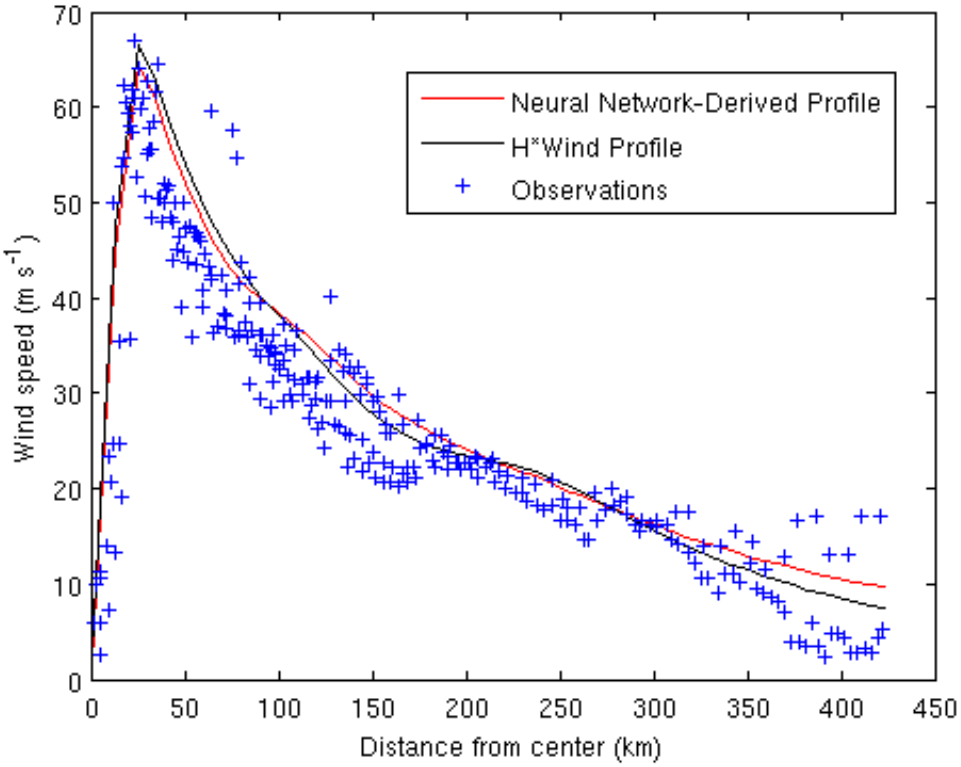

Figure 5: Neural network output. A neural network-derived radial profile of wind speeds in the right-front quadrant of Hurricane Ivan is plotted against the observations. The corresponding H*Wind profile (21Z 13 Sep 2004) is also plotted for comparison.

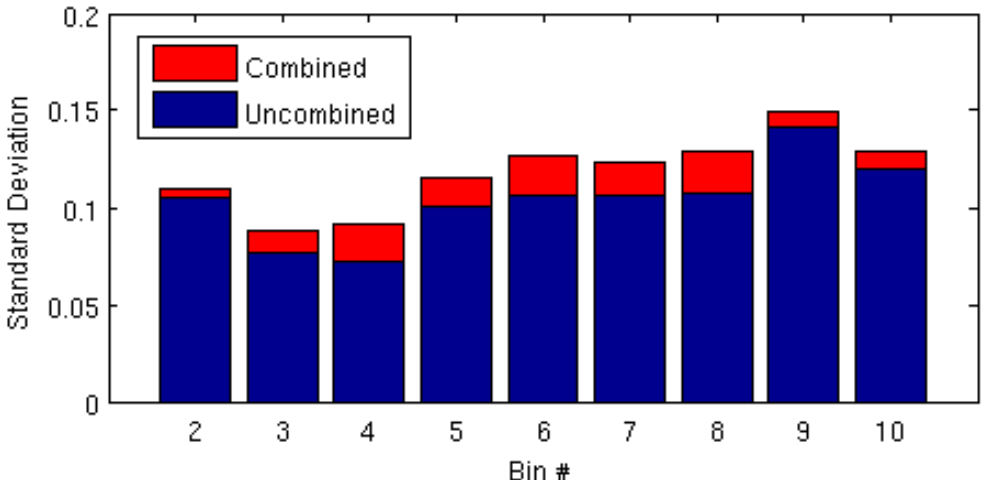

Figure 6: Neural network performance. The standard deviation of the scaled wind speed observations for each radial bin is plotted before (blue) and after (red) combining the observations into a single dataset.

biases and variability in the data. After the wind speeds are scaled, the effectiveness of the neural network technique as a scaling tool is analyzed by determining how much variability is added to the dataset when the storm analyses are combined. The standard deviation of the scaled wind speeds in each bin is calculated separately for each storm and compared to the standard deviation when all of the analyses were combined. The standard deviation of the combined dataset is up to 15% higher than the mean of the standard deviations of the individual storm analyses (figure 6). This increase represents the inter-storm variability that the scaling procedure failed to remove from the combined data set.

CHAPTER 5

EVALUATION OF BIASES AND RANDOM ERRORS

After the wind speeds from each observation are scaled to a non-dimensional number and the data from each analysis is combined into a single dataset, the mean and standard deviation are calculated for each observation platform in each radial bin. A significant difference in the means between two or more observation platforms within any given bin signifies a relative bias between those platforms. The standard deviation of each data type represents the total variability for that platform and bin. This variability represents the sum of random observation errors and temporal variations within the analysis windows, which contribute to the uncertainty in the H*Wind analyses, as well as spatial variations caused by binning the data and the inter-storm variability introduced by combining data from multiple analyses. Since the latter two sources of variability do not contribute to the uncertainty of H*Wind, the total uncertainty in H*Wind is slightly lower than the values reported in this analysis.

Figure 7 shows the mean and standard error of the scaled wind speeds for five observation platforms as well as the H*Wind analysis grid points as a function of radius. These five platforms include surface-adjusted air force reconnaissance data (AFRC), SFMR data from two NOAA aircraft, GPS dropsonde observations (GPSSonde), and SeaWinds data from the

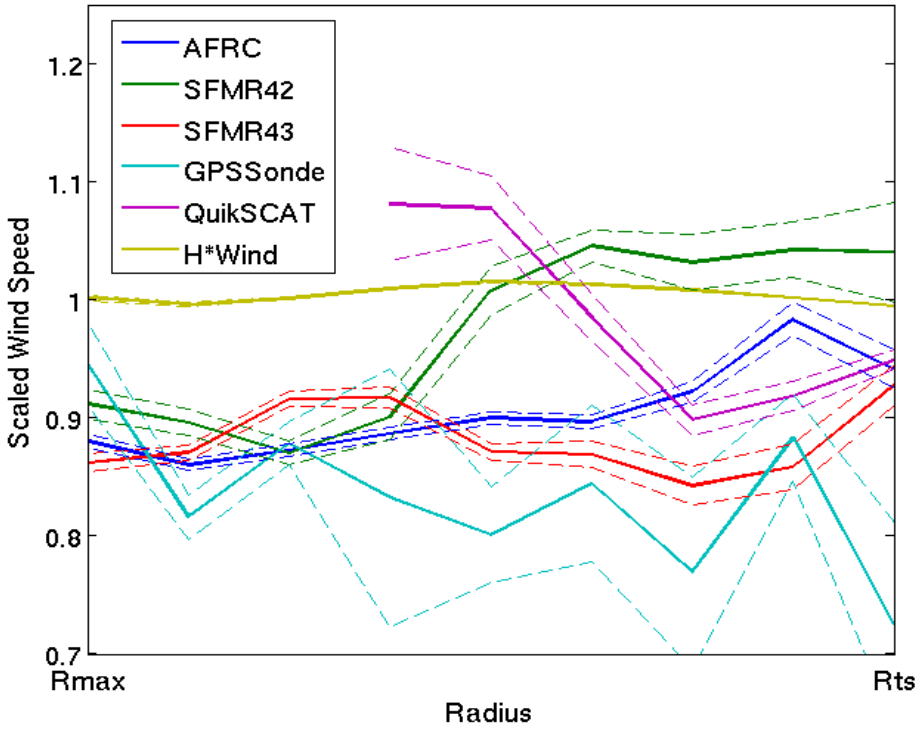

Figure 7: Mean of scaled wind speeds as a function of radius. The solid lines show the mean of the scaled wind speeds for five observation platforms in each of nine radial bins between the radius of maximum wind (Rmax) and the tropical storm force wind radius (Rts). The dashed lines show the mean plus and minus the standard errors of the means.

QuikSCAT satellite. A mean of one in fig.7 signifies a wind speed equal to the neural network profile wind speed. Since H*Wind is used to train the neural network, the mean of the scaled H*Wind speeds remains close to one; however, the mean scaled wind speed of most of the observation platforms near the eyewall is approximately 0.9, indicating that the H*Wind grid points have a positive bias of approximately 10% in this area. This large bias near the center is caused by H*Wind's enhancement algorithm, which enhances the H*Wind profile to equal the maximum observed wind speed in the eyewall, and not the mean. Away from the center, there is still an overall slight positive bias, but this is reflected accurately by the mean bias statistic reported by the H*Wind product.

Very little bias is found between the observation platforms near the storm center, indicating that the data is in strong agreement where it is most important operationally. Approximately one-third of the way between the R_{max} and R_{ts}, the biases between the observation types begins to increase substantially, adding uncertainty to the H*Wind analyses. QuikSCAT unsurprisingly experiences problems with rain contamination. Near the storm center, where the rain is heaviest, most of the observations were properly removed by the QuikSCAT rain-flagging algorithm. Unfortunately, the algorithm was less effective in the middle bins, where the rain is more scattered. Numerous rain-contaminated observations in the middle bins were therefore missed by the algorithm, resulting in wind speeds biased 10-20% higher than the other data platforms. This bias decreases on the far outside of the storm as the rain rate decreases. Also, one of the two aircraft taking SFMR measurements has a positive bias in the outermost bins. According to NOAA's Hurricane Research Division, the NOAA42 aircraft was not used operationally during much of the 2005 hurricane season, and was instead used to fly research missions (Uhlhorn and Klotz 2010, personal communication). This data therefore should have been discarded from the H*Wind database. Finally, the GPS dropsonde observations generally

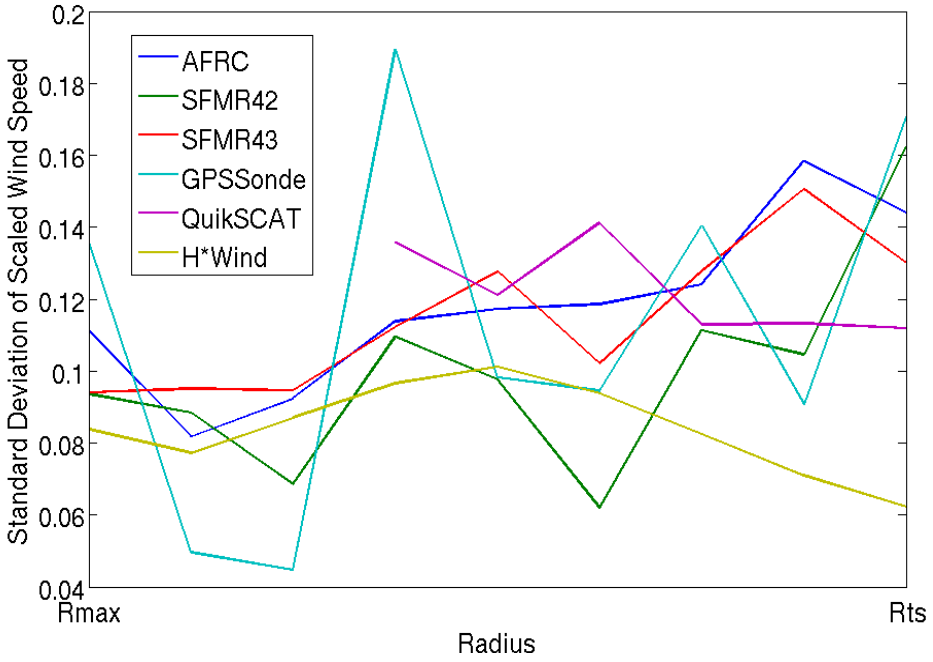

Figure 8: Standard deviation of scaled wind speeds as a function of radius. The standard deviations of the means of each data type in fig. 7 are plotted as a function of radius.

show a negative bias outside of the eyewall; however, the density of dropsonde observations in this region is extremely small, resulting in large standard errors, which render this bias statistically insignificant.

The standard deviations of the scaled wind speeds for each data type (figure 8) generally range between 0.07 and 0.15, which represents uncertainties of 7-15%. The smallest variability is generally found in near the storm center, again indicating that the data is most reliable near the eyewall, where it is crucial toward determining the storm intensity. The variability of most data types increases toward the outside of the tropical cyclones. This increase is caused by the larger distance between observations in this region, as well as the larger area covered by the binning scheme. An exception to this trend is the H*Wind analysis grid points, in which the standard deviation begins to decrease approximately halfway between R_{max} and R_{ts}. This decreased variability is caused by heavy smoothing of the H*Wind field in this region, which results in H*Wind being unable to resolve small-scale variations. The effects of smoothing are discussed in detail in Chapter 6. Finally, the standard deviations of the GPS dropsonde and NOAA42 SFMR observations are extremely erratic, reflecting the low density of GPS dropsondes and the non-operational use of the NOAA42 aircraft.

In order to determine whether any azimuthal trends exist in the uncertainties and biases for each observation type, the data are binned by azimuth relative to the storm motion vector and the calculations are repeated. Four bins are created, representing the right-front (RF), left-front (LF), right-rear (RR), and left-rear (LR) quadrants. Figure 9 shows the mean and standard error of each data type under the tangential binning scheme. QuikSCAT shows a strong positive bias in the right-front quadrant as a result of rain contamination, and H*Wind has a positive bias throughout due to its enhancement algorithm. Otherwise, the observation platforms are in

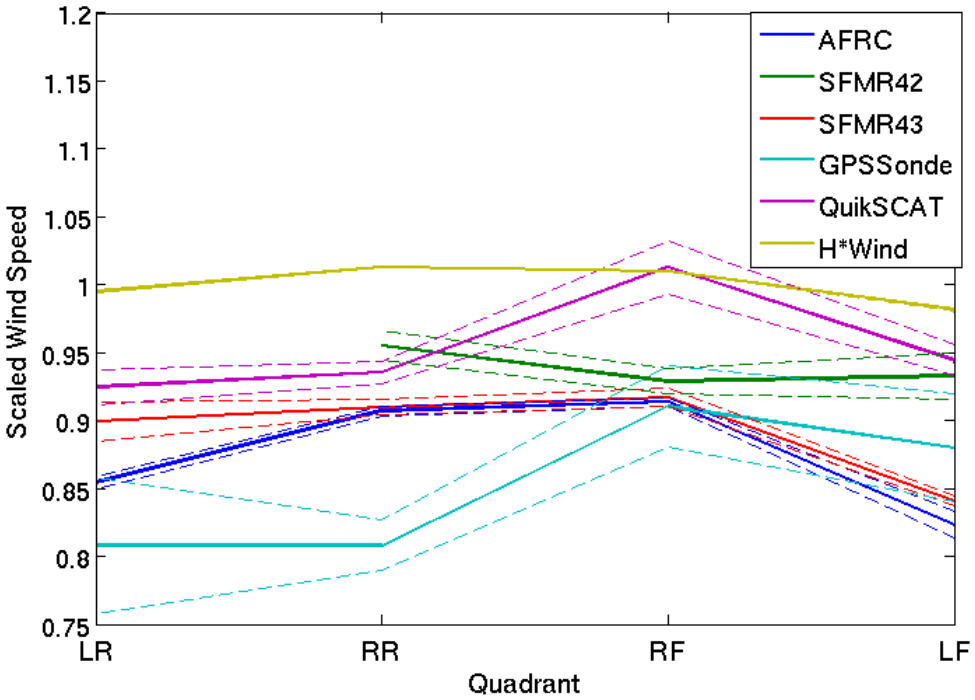

Figure 9: Mean of scaled wind speeds in each quadrant. This figure is the same as fig. 7, except that the data is binned by quadrant relative to the storm motion vector.

remarkably close agreement to each other in the right-front quadrant. Larger biases are found in the two left quadrants, particularly in the air force reconnaissance data, which has a negative bias in these quadrants. The standard deviations of the scaled wind speeds (figure 10) are generally highest in the front quadrants, due to the larger natural variability in this area. The H*Wind grid points reflect this same trend, but underestimate the variability as a result of smoothing.

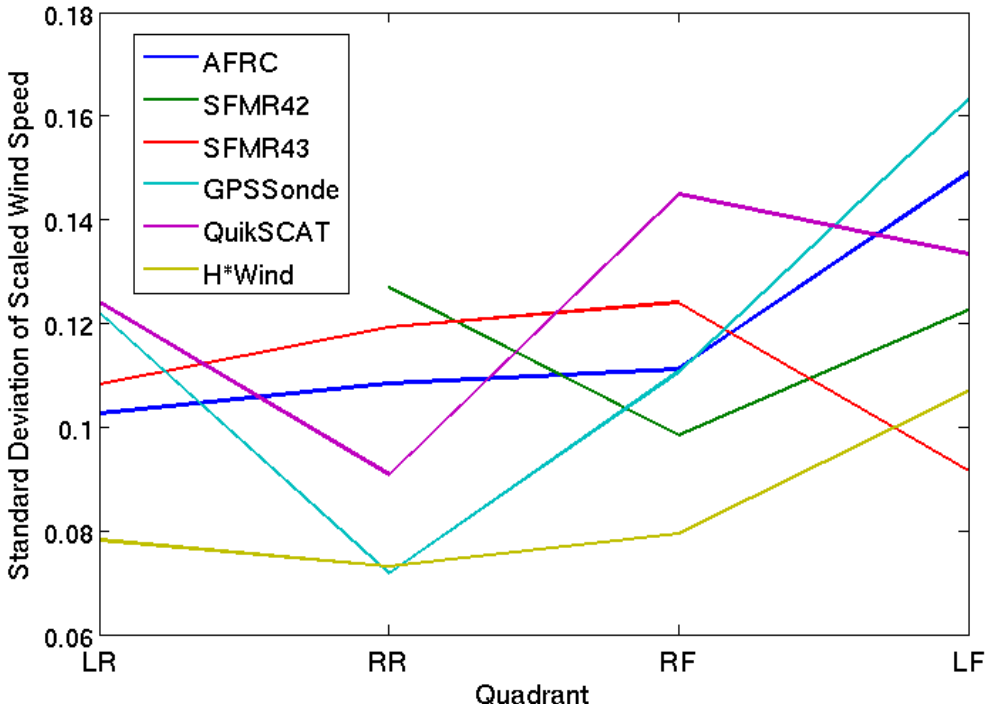

Figure 10: Standard deviation scaled wind speeds in each quadrant. This figure is the same as fig. 7, except that the data is binned by quadrant relative to the storm motion vector.

CHAPTER 6

SPECTRAL ANALYSIS

In order to determine the effects of smoothing on the H*Wind analyses, several spectral analyses were done on the H*Wind grid points to ensure that the resolution in both the radial and tangential directions matches the pre-specified values. Accurate resolution in H*Wind is critical when studying storm structure and in computer modeling applications. Radial spectral density is calculated at varying azimuths to determine whether the resolution of H*Wind had any tangential dependency. Similarly, tangential spectra are analyzed at several different radii to determine the presence of radial dependency. Since the H*Wind grid points are defined on a rectangular grid, some of the spectral analyses necessitate the interpolation of wind speeds at locations in between the grid points. A two-dimensional cubic spline interpolation is used to approximate the wind speeds in these cases.

Radial power density spectra for five H*Wind analyses are plotted in figure 11. Generally, the spectra of wind observations, when plotted on a log-log scale, have a nearly constant downward slope as wavelength decreases (Freilich and Chelton, 1986). A steepening of the slope signifies the presence of smoothing at the corresponding wavelengths, and noise will cause the spectra to level off. The five analyses plotted in fig. 11 each undergo the most smoothing between 15 km and 50 km. This range occurs contains the pre-specified filter wavelengths of the two innermost analysis meshes of these analyses (approximately 33 km and 43 km). H*Wind is able to resolve variability at wavelengths smaller than 33 km in the

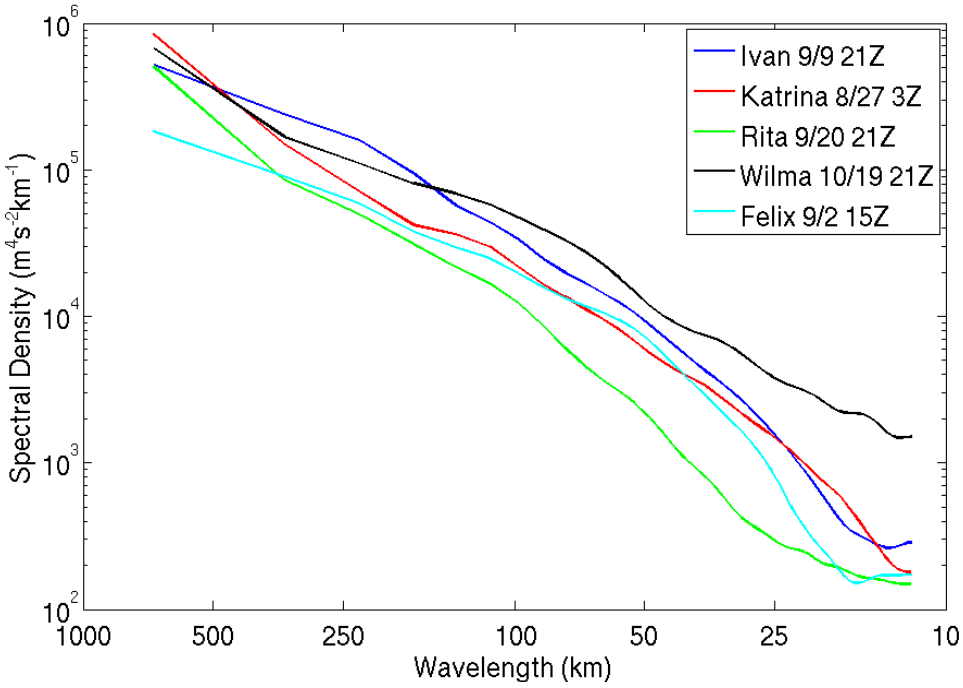

Figure 11: Radial spectra of H*Wind analyses. Power spectra are plotted as a function of wavelength for five H*Wind analyses at a 180° azimuth relative to the storm motion vector.

immediate vicinity of the eyewall as a result of the enhancement scheme.

There is some variation in the wavelengths at which smoothing occurs in the various analyses, even though each analysis has the same pre-specified filter wavelengths. Much of this variation is caused by the observation density in each individual storm. The analyses of well-sampled storms (e.g. Katrina) generally have slightly lower filter wavelengths than those of poorly sampled storms. Some of this variability in filter wavelengths is also caused by the structural characteristics of each storm, such as the radius of the eyewall. Changing the azimuth of the spectra in fig. 11 (not shown) has very little effect on the results. The power spectral density is slightly lower at all wavelengths for azimuths other than the four cardinal directions as a result of interpolation between grid points, but this effect is negligible when compared to the spread of the spectral plots for different storm analyses.

Tangential spectra at radii of 50 and 200 km are shown in figures 12 and 13, respectively. At a 50 km radius, the preset filter wavelength in H*Wind is approximately 40 km. The spectra in figure 12, although jagged, generally show smoothing in the 25-75 km range. Again, there is some variation among the analyses due to differences in data coverage, but there is no discernable signal left at wavelengths below 25 km. At a 200 km radius, data is much more sparse, and so the H*Wind filter wavelength is set to approximately 170 km. The spectra in figure 13 show that smoothing begins to occur at this wavelength, and the signal deteriorates rapidly thereafter. Several spikes are present in both the 50 km and 200 km tangential spectra as a result of the non-uniform distribution of observations within the storms. Reconnaissance aircraft data, for example, is only found along the flight path. The circular paths that the tangential spectra are taken along cross the reconnaissance aircraft flight path several times, and

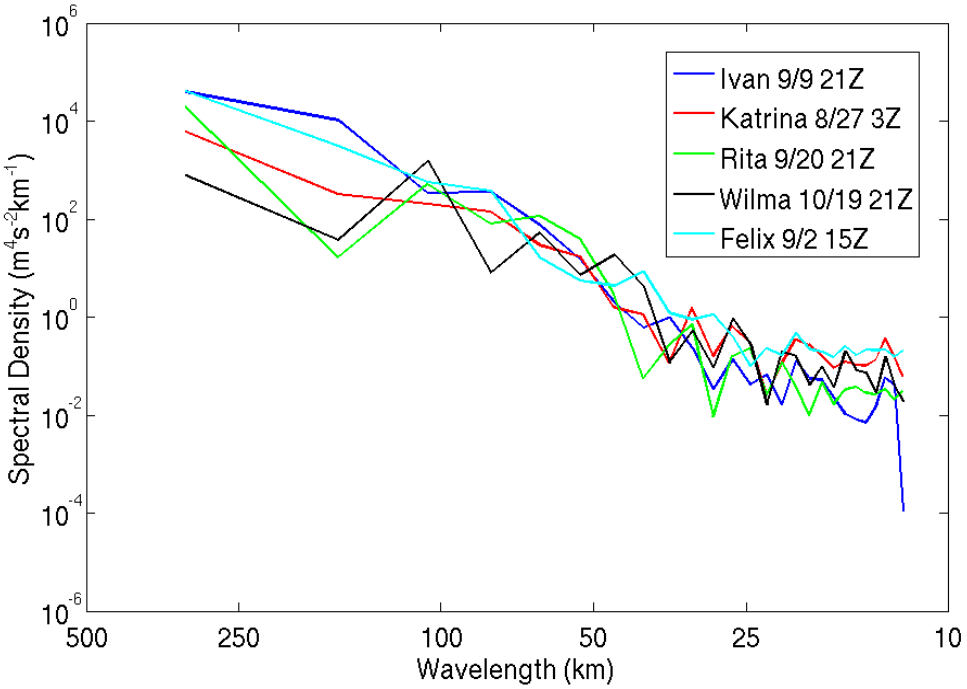

Figure 12: Tangential spectra of H*Wind analyses at a 50 km radius. Power spectra are plotted as a function of wavelength for five H*Wind analyses. The spectra are calculated along a swath of interpolated H*Wind data points at a constant 50 km radius from the storm center.

therefore contain many large fluctuations in observation density. In regions where the observation density is high, such as along a radial flight leg, the analysis resolution is also high; meanwhile much more smoothing takes place in data-sparse regions, resulting in a poor analysis resolution. The presence of spikes in the tangential spectra signifies that availability of observations is a major limiting factor in the resolution of H*Wind analyses; this is in agreement with Franklin, et al. (1993).

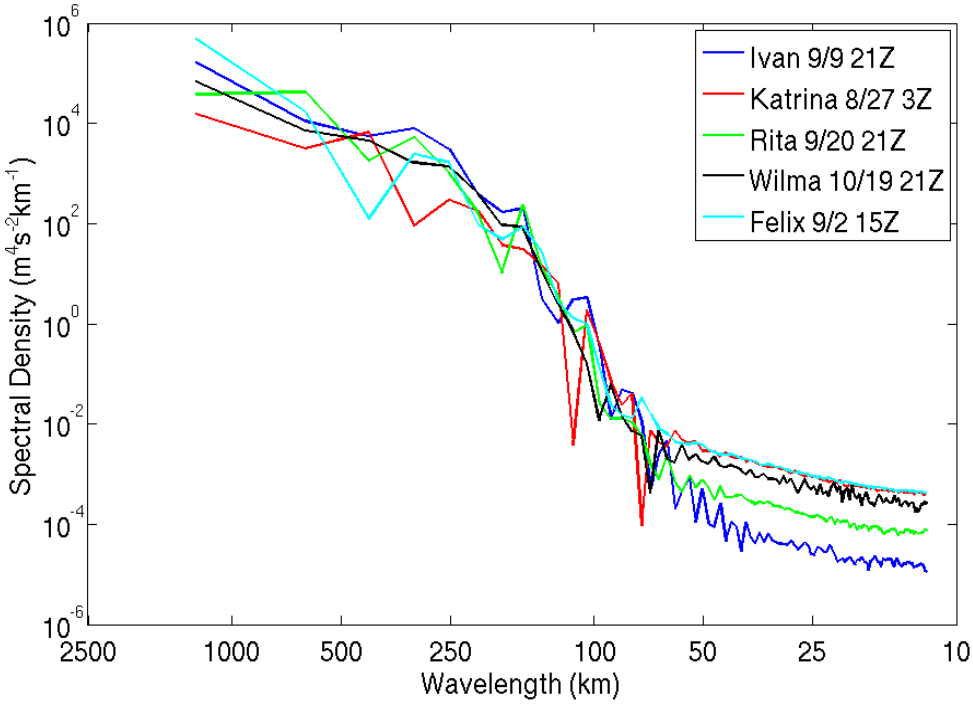

Figure 13: Tangential spectra of H*Wind analyses at a 200 km radius. Same as figure 12, except that the spectra are calculated at a constant radius of 200 km from the storm center.

CHAPTER 7

CONCLUSIONS

The observational random errors and biases are estimated for several tropical cyclone wind observation platforms. In the absence of large relative biases, the total variability within the observations at a particular radius generally ranges from 7-15% with larger values in front of the storms, where more natural variability is found. Since some of this variability is artificially created by combining data from multiple storm analyses and by binning the data, the combined total of the observation errors and temporal variability are smaller than 15% in the absence of bias. A significant bias is found in the QuikSCAT observations as a result of rain contamination, indicating that the near real time QuikSCAT rain-flagging algorithm only captures the seriously contaminated observations. Additionally, a significant positive bias is found in the SFMR observations as a result of non-operational use of the NOAA42 aircraft during the 2005 season. Each of these observation errors are carried into the H*Wind analyses and contribute to the errors in the gridded product.

The H*Wind algorithm also adds some bias to the analyses. A large positive bias occurs near the eyewall due to the enhancement to the maximum observed wind speed. Away from the eyewall, H*Wind accurately reports the bias for each individual analysis. Most of the small-scale variations in the observations are smoothed away by H*Wind, especially near the outer fringes of the storm. Although the preset filter wavelengths in H*Wind can be changed to improve resolution, observation density remains a limiting factor, and generally makes H*Wind unsuitable for resolving the wind anomalies associated with small-scale features, including outer rain bands. Other issues noted with the H*Wind analyses are their inability to resolve multiple radial peaks without adding large amounts of noise to the analysis product and its inability to account for smaller scale temporal variability due to averaging over a 4-6 hour time window. These issues limit the usefulness of H*Wind in storms with concentric eyewalls and in cases of rapid intensification.

H*Wind therefore provides a first guess of the intensity and size of tropical cyclones, but lacks the accuracy and resolution desired for several research applications (e.g., satellite calibration). Differentiating between radial and tangential filter wavelengths may help resolve more of the natural radial variability in tropical cyclones without adding unrealistic noise in the tangential direction. In addition, a tangentially dependent enhancement scheme can help resolve tangential variability within the eyewall. More quality control is clearly needed to remove or adjust heavily biased observations in the H*Wind database, and a time parameter is needed to handle changes in storm structure and intensity within an analysis time window. There have been several suggestions for improving the product, such as a more advanced analysis algorithm using an ensemble Kalman filter.

REFERENCES

Dunion, J. P., S. H. Houston, C. S. Velden, and M. D. Powell, 2002: Application of surface-adjusted GOES low-level cloud-drift winds in the environment of Atlantic tropical cyclones. Part II: integration into surface wind analyses. *Mon.Wea. Rev*. **130**, 1347–1355.

Franklin, J. L., M. L. Black, and K. Valde, 2003: GPS dropwindsonde wind profiles in hurricanes and their operational implications. *Wea. Forecasting*, **18**, 32–44.

Franklin, J. L., S. J. Lord, S. E. Feuer, and J. D. Marks, Jr., 1993: The kinematic structure of Hurricane Gloria (1985) determined from nested analyses of dropwindsonde and Doppler radar data. *Mon. Wea. Rev.*, **121**, 2433-2451.

Freilich, M. H. and D. B. Chelton, 1986: Wavenumber spectra of Pacific winds measured by the Seasat scatterometer. *J. Phys. Oceanogr.*, **16**, 741-757.

Halliwell, G. R. Jr., L. K. Shay, S. D. Jacob, O. M. Smedstad, and E. H. Uhlhorn, 2008: Improving ocean model initialization for coupled tropical cyclone forecast models using GODAE nowcasts. *Mon. Wea. Rev.*, **136**, 2576-2591.

Holland, G. J., 1980: An analytic model of the wind and pressure profiles in hurricanes. *Mon. Wea Rev.*, **108**, 1212-1218.

Landsea, C. W. et al., 2004: A reanalysis of Hurricane Andrew's intensity. *Bull. Amer. Meteor. Soc.*, **85**, 1699-1712.

Liu, W. T., K. B. Katsaros, and J. A. Businger, 1979: Bulk parameterizations of air-sea exchanges of heat and heat and water vapor including the molecular constants at the surface. *J. Atmos. Sci.*, **36**, 1722–1735.

Morey, S. L., S. Baig, M. A. Bourassa, D. S. Dukhovskoy, and J. J. O'Brien, 2006: Remote forcing contribution to storm-induced sea level rise during Hurricane Dennis. *Geophys. Res. Letts.*, **33**, L19603-19607.

Powell, M. D., and S. H. Houston, 1996: Hurricane Andrew's landfall in South Florida. Part II: Surface wind fields and potential real-time applications. *Wea. Forecasting,* **11**, 329-349.

Powell, M. D., S. H. Houston, L. R. Amat, and N. Morisseau-Leroy, 1998: The HRD real-time hurricane wind analysis system. *J. Wind Eng. Indust. Aerodyn.*, **77–78**, 53–64.

Powell, M. D., S. H. Houston, and T. A. Reinhold, 1996: Hurricane Andrew's landfall in South Florida. Part I: Standardizing measurements for documentation of surface wind fields. *Wea. Forecasting*, **11**, 304-328.

Powell, M. D., S. Murillo, P. Dodge, E. Uhlhorn, J. Gamache, V. Cardone, A. Cox, S. Otero, N. Carrasco, B. Annane, and R. St. Fleur, 2009: Reconstruction of Hurricane Katrina's wind fields for storm surge and wave hindcasting. *Ocean EngI.*, **37**, 26-36.

Powell, M. D., E. W. Uhlhorn, and J. Kepert, 2009: Estimating Maximum Surface Winds from Hurricane Reconnaissance Measurements. *Wea. Forecasting*, **24**, 868-883.

Uhlhorn, E. W., and P.G. Black, 2003: Verification of remotely sensed sea surface winds in hurricanes. *J. Atmos. Oceanic Technol.,* **20,** 99–116.

Uhlhorn, E. W., P.G. Black, J. L. Franklin, M. Goodberlet, J. Carswell, and A. S. Goldstein, 2007: Hurricane surface wind measurements from an operational stepped frequency microwave radiometer. *Mon. Wea. Rev.*, **135**, 3070–3085.

Vickery, P. J., and D. Wadhera, 2008: Statistical models of Holland pressure profile parameter and radius to maximum winds of hurricanes from flight-level pressure and H*Wind data. *J. Appl. Meteor.*, **47**, 2497-2517.

Willoughby, H. E., R. W. R. Darling, and M. E. Rahn, 2006: Parametric representation of the primary hurricane vortex. Part II: A new family of sectionally continuous profiles. *Mon. Wea. Rev.*, **134**, 1102-1120.

Xiao, Q., X. Zhang, C. Davis, J. Tuttle, and G. J. Holland, 2008: Experiments of hurricane initialization with airborne Doppler radar data for the advanced research hurricane WRF (AHW) model. *Mon. Wea. Rev.*, **137**, 2758-2777.

BIOGRAPHICAL SKETCH

Steven DiNapoli was born in St. Louis, Missouri on September 13, 1985. As a child, he moved across the country with his family several times, spending time in Ohio, Illinois, California, Oregon, and most recently, the Atlanta area. Steven developed an interest in weather at an early age, and has desired to become a meteorologist since grade school. After graduating from high school in 2004, Steven entered the Georgia Institute of Technology and majored in Earth and Atmospheric Sciences. After receiving his Bachelor's degree in 2008, Steven received a University Fellowship from Florida State University and began pursuing his Master's degree in Meteorology.

Steven enjoys weather forecasting and he has participated in the WxChallenge national collegiate weather forecasting competition since the fall of 2006. He placed in the top 25 forecasters nationally in the 2008-09 and 2009-10 academic years, and has received national recognition for his forecasting excellence.